SAND99-1293 J

CALCULATION OF SHIPBOARD FIRE CONDITIONS

J.A. Koski and S.D. Wix

Transportation Technology Department, Sandia National Laboratories, Albuquerque, NM

J.K. Cole

Aerosciences and Compressible Fluid Mechanics Department, Sandia National Laboratories, Albuquerque, NM

TS 9711-636

DISCLAIMER

Portions of this document may be illegible in electronic image products. Images are produced from the best available original document.

Successful techniques have been developed for simulating some experimental shipboard fires. The experimental fires were staged in Holds 4 and 5 of the *Mayo Lykes*, a test ship operated by the United States Coast Guard Fire and Safety Test Detachment at Little Sand Island in Mobile Bay, Alabama. The tests simulated an engine-room or galley fire in the compartment adjacent to simulated hazardous cargo. The purpose of these tests was to determine the effect the fires in Hold 4 had on the cargo in Holds 4 and 5. The simulation is done with CFX, a commercial computational fluid dynamics code. Analyses show that simulations can accurately estimate a maritime fire environment for radioactive materials packaging. Radiative heat transfer dominates the hold-fire environment near the hot bulkhead. Flame temperatures between 800 and 1000°C give heat fluxes and temperatures typical of the measured fire environment for the simulated radioactive materials package. The simulation predicted the occurrence of flow patterns near the calorimeter (simulated radioactive materials package) similar to those observed during the experiment. The simulation was also accurate in predicting a heated fluid layer near the ceiling that increases in thickness as time passes.

INTRODUCTION

Radioactive material shipments have raised concerns about safety in the face of shipboard fires [1]. A series of tests conducted aboard an actual freighter with simulated radioactive materials packages improved the knowledge of the shipboard fire environment [2]. If computer models of these tests can be developed and proven to be accurate, then the computation methods developed can be applied with confidence to other shipboard fire geometries, sizes, and durations. The computer models described here include conduction, convection, and thermal radiation. This paper provides information on the success and accuracy of the model simulations compared to the experimental results from the actual shipboard fires [2,3].

A commercially available computational fluid dynamics computer code CFX [4] has been used for the calculations. This code was selected because of its previous use in fire analyses and its ability to treat all heat transfer mechanisms, i.e., conduction, convection, and thermal radiation, in a coupled manner. In addition, an effort has been made to limit the input of experimental results into the analytical model so that analysts without access to detailed experimental data can confidently create similar models.

This paper documents successful techniques for simulating some experimental shipboard fires. The experimental fires were staged in Holds 4 and 5 of the *Mayo Lykes*, a 10700 deadweight ton World War II, Liberty Class, break-bulk freighter (Figures 1 and 2). The U.S. Coast Guard Fire and Safety Test Detachment at Little Sand Island in Mobile Bay, Alabama, operates such ships for fire test purposes. The results from three tests in the experimental series were selected for analysis [2]. The experimental fires, designated Tests 5037 and 5045, were two-burner and four-burner heptane spray tests with the ignited sprays impinging on the Hold 4-5 bulkhead. These tests simulated an engine-room or galley fire in an adjacent compartment. The purpose of these tests was to determine the effect the fires in Hold 4 had on simulated hazardous cargo in Hold 5.

Test 5040, a wood crib fire in Hold 4, simulated burning cargo in the same hold as the hazardous cargo. Simulations of this test emphasized the conditions in Hold 4.

The general layouts of Level 1 of Holds 4 and 5 are shown in Figures 3 and 4. These holds are located just below the weather deck of the ship. The Engine Room mock-up is a sheet metal structure used for fire-suppression tests. The king post (mast), centered in the Hold 4-5 bulkhead, is a large circular steel structure supporting a cargo crane located on the weather deck of the *Mayo Lykes*. Hold 5 contains a large furnace intended for other fire experiments aboard the *Lykes*. Height of the holds varied, but was approximately 3.7 m. Ventilator ducts in Holds 4 and 5 (see Figures 3 and 4) were removed before the fire experiments to simplify the problem geometry and remove obstacles to heat transfer between the holds.

Ventilation was provided to Hold 4 to prevent the accumulation of explosive gas mixtures in the holds. For the heptane-spray fires, the port and starboard openings in the hull were open, as were the openings at the forward end of the engine-room mock-up. Two 2 m x 3 m panels in the roof of the engine-room mock-up were also removed to provide vertical ventilation for the smoke. For the wood crib fires, the openings at the forward end of the engine-room mock-up were closed. For all tests, openings in Hold 5 were closed to simulate at-sea conditions for cargo.

COMPUTATIONAL FLUID DYNAMICS CODE AND BASIC ASSUMPTIONS

The CFX computer code chosen for these simulations is a finite volume, multi-block computational fluid dynamics code that can solve coupled energy and fluid transport problems [4]. Conduction and radiation solutions are treated simultaneously with flow solutions. Cartesian or cylindrical coordinates may be used to construct full three-dimensional models of solids and fluid-filled volumes. A standard k-e flow turbulence model [4] was used for the fire simulations with the SIMPLE [5] algorithm applied for numerical solutions. Buoyancy was included in the models because flow is induced by natural convection. A weakly compressible buoyancy model was used, in which density is a function of temperature.

Thermal radiation solutions in CFX were achieved with the Shah model [4]. No attempt was made to model the chemical reactions in the combustion processes of the heptane sprays or wood cribs. Instead, total fire energy outputs estimated by Koski et al. [2] were used in surface and volumetric models of the bulkhead and wood cribs as described below. In addition, for most cases, air was assumed to be the working medium, with no attempt to model the gaseous combustion products. Where described, grey-gas participating-medium radiative-heat-transfer models were used to determine the possible effects of smoke in Hold 4.

For numerical convergence, enthalpy of the air was selected as the most important parameter. Implicit time stepping was used for all solutions, and the correctness of the size of the time step was confirmed through checks against results from solutions with smaller time steps.

This page intentionally left blank.

DESCRIPTION OF HOLD AND FIRE MODELS

Hold 4 Model. Hold 4 of the *Mayo Lykes* is located one level below the weather deck, aft of the superstructure, and immediately forward of Hold 5. The arrangement of the hold is symmetrical with respect to the ship's longitudinal axis. This symmetry was maintained during the fire tests by positioning the centerlines of the fire and the calorimeter on the ship's centerline. Asymmetric thermal or flow processes that violate this symmetry were not included in the model.

The starboard (right) half of Hold 4 was modeled in the CFX code (Figure 5). Symmetrical flow conditions were also assumed for the CFX calculations for Hold 5 discussed below, but the port (left) side was modeled in that case. This difference is not important so long as information being transferred between these models is reflected properly about the plane of symmetry. Figure 6 expands the view of the region of Hold 4 in which the fire was located.

The orthogonal coordinate system used to describe the model has its origin at the lower rear inside corner of the hold, where the plane of symmetry intersects the rear bulkhead and the deck. The X-axis is defined as parallel to the ship's longitudinal axis and positive toward the bow. The Y-axis is positive upward, and the Z-axis is positive toward the starboard side. Figure 7 shows plan and elevation views of Hold 4. The thicknesses of the bulkheads, deck, and overhead are exaggerated to make their dimensions easy to identify.

The bulkheads were 0.0082 m thick, the deck and overhead were 0.0107 m thick, and the hull was 0.0181 m thick. These were all modeled as conducting solids made of mild steel with the following properties: density = 7837 kg/m^3; specific heat = 460 J/(kg K); conductivity = 45 W/(m K).

The outer surfaces of Hold 4, i.e., the bulkheads, deck, and overhead, were subjected to convective and radiative heat transfer assuming a constant atmospheric temperature of 303 K. The radiative emissivity was 0.8 for these outer surfaces. The convective heat-transfer coefficients were varied depending on the orientation of each surface. The values used were the following: vertical surface of bulkhead or hull = 1.58 W/(m^2 K); lower surface of deck = 1.05 W/(m^2 K); upper surface of overhead = 2.00 W/(m^2 K).

Shear stresses at the inner surfaces of the bulkheads, deck, and overhead were left unspecified so that the CFX code would force the fluid velocity to zero at each of these surfaces. The plane of symmetry was also treated as a wall except for the shear stresses being set to zero. This permitted non-zero fluid velocity components parallel to the plane of symmetry.

A king post is integrated with the bulkhead separating Holds 4 and 5 so that approximately half of it extends into each hold. The portion in Hold 4 was reinforced with large trapezoidal steel plates welded to both sides of the king post. The resulting shape approximates a rectangular object more closely than a half cylinder. The actual king post is hollow, but to simplify the CFX model, the king post in the simulation was assumed to be a conducting, rectangular solid. To give the model king post the same thermal mass and thermal diffusivity as the real one, its

thermal properties were modified as follows: density = 520 kg/m^3; specific heat = 460 J/(kg K); conductivity = 3.06 W/(m K).

Wood Crib Fire Model. The model of the burning wood crib included both radiative and convective parts (Figure 8). The radiative parts were the lateral and top faces of the wood crib, the plume wall radiator in the plane of symmetry, and the plume center radiator that extended from the top of the crib to the overhead. The convective part was the air volume between the top of the wood crib and the overhead. The crib was assumed to maintain its original shape through the entire burn.

The wood crib was constructed of 2 x 4's, i.e., Douglas fir boards 0.04 m x 0.09 m x 1.58 m. These were laid in alternating layers with the lengths of the boards in each layer at right angles to those in the adjacent layers. In the model the wood was assumed to reach a steady burn 30 seconds after ignition and to burn at a constant rate for 1170 seconds. The crib then returned to zero energy output in 300 seconds. In the experiment, a heptane accelerant was used at the beginning of the wood fire. The model assumed that the accelerant was reached a steady burn within 30 seconds, burned steadily for 270 seconds, and was extinguished within 30 seconds. The maximum rate of thermal energy released by the wood and the accelerant was calculated to be 2.37 MW and 1.73 MW, respectively. These whole fire values were halved for the simulation of the starboard half of the hold.

The first attempt to model the fire assumed that the lateral and upper surfaces of the crib remained at a constant temperature of 473 K from ignition until burnout, while the plume radiated most of the energy to the surroundings. Temperatures calculated for the calorimeter using this fire model were much lower than the experimental data.

The second attempt to model the fire assumed that the crib contributed substantially in releasing energy as a radiant heat source. The calculated maximum heat released from the wood crib and the heptane accelerant during the first 300 seconds of the burn was divided about equally between convective and radiant heat transfer. The radiant heat release of the wood crib was then held at this same level until burnout commenced at 1200 seconds. This approach gave better results than the first attempt, and those results are reported here.

The outer surfaces of the wood crib were assigned an emissivity of 0.5 and the plume surfaces, 0.9. A maximum fire temperature of 1190 K was required to release the correct radiant heat flux during the period of steady burn. At this temperature the wood crib radiated at 56.9 kW/m ^{2} and the plume surfaces at 102.3 kW/m ^{2}.

The surfaces of the plume wall radiator and the plume center radiator were assigned zero shear stresses. This permitted air near these surfaces to flow parallel to them, but not through them.

The large transient due to the heptane accelerant was assigned almost entirely to the convective heat release. The convective energy was deposited directly into the air volume between the top of the crib and the overhead. This enhanced the transfer of heat to the air and encouraged the formation of convection. This energy deposition decreased from about 354 to 66 kW/m ^{3} as the accelerant burned out at 300 seconds. Figure 9 shows the heat flux versus time for the total

energy released as well as the energy partitioning between radiation and convection that was used in the model. All of the transients in energy release were modeled with half-cycle cosine functions.

Simulation of Smoke Effects. The wood crib fire experiments on the *Mayo Lykes* generated considerable smoke. To approximate the decreased transparency of the air caused by this smoke, the absorptivity of the air was made a function of air temperature. Geophysical data indicated that clear air had an absorptivity around 6×10^{-5} m^{-1} and light fog, an absorptivity around 6×10^{-3} m^{-1} [6]. If one assumes that the smoke was associated with the hotter air, an S-shaped function can be defined that varies the air absorptivity between zero absorptivity at 300 K and an absorptivity of 10 m^{-1} at 1200 K in approximate agreement with the geophysical data. This function is shown in Figure 10. At 300 K, the optical depth is essentially infinite and at 1200 K it is decreased to 0.1 m. Fire solutions were calculated with the smoke model and with air that was essentially transparent with an absorptivity of 1×10^{-3} m^{-1}.

Calorimeter Model. The experimental calorimeter was made from a steel pipe with a wall thickness of 0.025 m, an outside diameter of 0.61 m, and a length of 1.5 m. Its ends were covered by steel disks, 0.025 m thick, and its interior was filled with insulation. In the CFX simulation, the right half of this calorimeter was modeled as a steel cylinder of the proper dimensions with an insulated interior. An end cover was not included in the model, because it has little influence on the temperatures of the steel cylinder in the side-on orientation to the fire used in the tests.

The calorimeters were instrumented with thermocouples to permit determination of temperatures and heat transfer to the calorimeters. The calorimeters in Holds 4 and 5 are identical, and most thermocouples were located on the side facing the hot bulkhead between the holds. To analyze the data from the experiments, the SODDIT computer code [7] was used to calculate the heat flux to the surface of the calorimeter based on the temperatures obtained from the thermocouples. Material properties for carbon steel are necessary for estimation of heat fluxes from temperature data. For the analysis, the interior surface of the calorimeter was assumed to be insulated to avoid the necessity of performing complicated radiative-heat-transfer calculations of the interior pipe cavity.

For consistency in comparison of the analytical results to the experimental heat fluxes, the SODDIT code was also used to estimate the heat fluxes to the calorimeter from temperatures calculated with the CFX code.

Modeling of Openings. In the starboard half of Hold 4, a single inlet is located near deck level, and a single outlet is located near the top of the forward bulkhead of the engine room (Figures 5 and 7). The lower edge of the inlet penetrates the hull about 0.5 m below the deck, and several steps are required to reach deck level. The indentation in the deck created by the enclosed stairwell was not explicitly modeled. Instead the model contained an opening whose upper edge

was located at the same height above the deck as that of the actual entrance. The model inlet was made wider to provide the same flow area as the actual inlet. The model inlet was centered longitudinally in the hold.

The outlet was modeled with the same area and proportions as the actual outlet, but was placed in the overhead rather than at the top of the bulkhead. Initial CFX calculations assumed both inlet and outlet were open to flow and were constant-pressure boundaries. This resulted in cool outside air coming into the hold through the inlet and the heated air exiting through the outlet.

For the heptane fire tests, the inlet and outlet were open to prevent a buildup of explosive gas. However, the outlet in the overhead was closed for the wood-crib fire tests. Flow solutions were calculated for a wood-crib fire with the outlet open as well as closed. When the outlet was closed, air flowed into the hold through the lower part of the inlet and out through the upper part.

Radiation Model. The CFX code offers two methods for calculating the radiative heat transfer between surfaces, a Monte Carlo simulation and a discrete transfer method by Shah [4]. The problem considered here has a fixed, rather simple geometry and assumes grey-body radiation. The radiation field was expected to be reasonably homogeneous. Shah's method is the more suitable of the two under these conditions and, therefore, was used in this simulation.

Table 1 lists the radiative properties for the various surfaces in the hold. As the roughness parameter for surface increases from 0.0 to 1.0, its spectral reflection decreases linearly from 100% to 0 and its diffuse reflection increases linearly from 0 to 100%. Albedo indicates the reflectivity of a surface; a value of 0.2 indicates that 20% of the incident radiant energy is reflected and the rest absorbed.

TABLE 1. Radiative Properties

Surface	Albedo	Roughness
Bulkheads, Deck & Overhead	0.2	1.0
Plume & Crib	0.1	1.0
Symmetry Surface	0.0	0.0

Hold 5 Model Description. The computational fluid dynamics (CFD) model of Hold 5 is a three-dimensional symmetric model which contains 64,352 cells (Figure 11). Each cell is a volumetric representation of a portion of the model. As with Hold 4, an axis of symmetry at the ship centerline was used to reduce the overall size of the model. Conducting solids were used to model features such as the hold bulkheads, deck and overhead, the calorimeter, and the king post.

A radiation model of Hold 5 was also constructed to run simultaneously with the flow solver. The CFD model and the radiation model are coupled automatically to produce the interaction between convective, conductive, and radiative heat transfer. The CFD model transfers either temperatures or heat fluxes to the radiation model, depending on the type of wall boundary chosen. The radiation model solves the radiation problem by tracking photons through a set of zones that form the calculation domain. As with Hold 4, the Shah method was chosen for the radiative-heat-transfer calculations. The thermal emissivity of the bulkheads, deck, and overhead was assumed to be 0.75, and the radiative emissivity of the calorimeter was 0.8. All surfaces except the axis of symmetry wall had a surface roughness of 1.0. The surface roughness is the fraction of reflection which is diffuse; the remainder is assumed to be specular. Thus, all surfaces in the radiation model, except the axis-of-symmetry wall, were diffuse walls. For the axis-of-symmetry wall, the albedo was 1.0, which means that the axis-of-symmetry wall was assumed to be a perfect reflective surface. A grey-body radiation assumption was used in the model and the media within the flow model was nonparticipating.

The dimensions for the bulkheads in Hold 5 of the *Mayo Lykes* are the same as in Hold 4. The bulkheads are 0.0082 m thick, the deck and overhead are 0.011 m thick, and the hull is 0.018 m thick. The bulkheads, overhead, deck, and hull were modeled using conducting solids in order to include capacitance effects. A king post was present in the hold and was also modeled as a conducting solid. A furnace was also present in Hold 5 when the tests were performed. The furnace was assumed to be a thin sheet of metal covering a low capacitive, low thermal conductivity material such as fire brick. Based on the composition of the furnace, the walls of the furnace were assumed to be adiabatic and were modeled as non-conducting walls.

Boundary Conditions. An underlying assumption of this analysis is that the flame of the engine-room fire is in contact with the hold bulkhead and creates a localized hot spot on the bulkhead. The size and shape of the hot spot used in the analysis was taken from the experimental results from the *Lykes* experiments. Infrared images of the bulkhead were taken during the experimental heptane spray tests and the size of the hot spot was scaled from the infrared image (Figure 12). Since the king post diameter and the deck/bulkhead intersection are known, the approximate size and location of the hot spot on the bulkhead can also be determined. The hot spot was connected using radiation and convection to a boundary condition node set at a temperature source of 900°C, which is in the expected range of flame temperatures. A flame emissivity of 0.9 and a convection coefficient of 10 W/m ^{2}-°C were used.

A symmetry plane was used to model the axis of symmetry in the hold. The symmetry plane had a shear stress of zero to reflect the axis of symmetry in the flow field. With a shear stress of zero

at the axis of symmetry, the no-slip wall boundary condition was avoided and the flow was not influenced by the symmetry plane.

Natural-convection boundary conditions were assumed on the exterior of the hold. The convection coefficients depend on surface orientation. For the bulkheads, the convection coefficient was 4.63 W/m^{-2}. For the deck and overhead, the convective coefficients were 0.775 W/m^2 and 5.67 W/m^2, respectively. The ambient temperature for the two-nozzle calculation was 35°C. For the four-nozzle calculation, the ambient temperature was 15°C. The ambient temperature values were taken from the experimental data.

RESULTS

Hold 4 Model Results: Convergence and Sensitivity . For the simulation of the wood crib fire, time steps of different sizes were used for different parts of the burn. Smaller time steps were used when calculating through large transients in the fire's thermal output than for periods of constant thermal output (Table 2). The calculation of a solution from 0 to 1500 seconds took over 80 hours on an HP755 computer.

TABLE 2. Time steps used.

Time from start of fire (seconds)	Computational time step (seconds)
0 - 60	1.0
60 - 300	5.0
300 - 330	1.0
330 - 1200	5.0
1200 - 1500	1.0

To evaluate the sensitivity of the simulation to the choice of time step, a solution was found with time steps that were half as large as the time intervals shown in Table 2. A comparison of the surface temperatures on the cask at the 90-degree position, which looks directly at the burning wood crib, showed essentially no differences in results for the full and half time steps. A comparison of the air temperatures at three heights on a pole located in the hold more than 6 m from the fire was also made (Figure 13). This location exhibited an increased sensitivity to the time step parameter. At this location, little difference at the lowest position, 0.91 m above the deck, was detected, but differences up to 5°C at the highest position, 2.13 m above the deck, were calculated. Since the calorimeter results were well converged, and the 5°C difference was well within acceptable limits for air temperatures, the times steps in Table 3 were considered sufficiently accurate for the current solution.

Calorimeter and Hold Temperatures

Figure 14 shows an end view of the calorimeter with the angular locations for the thermocouples and for the calculated temperatures. The 0-degree location is at the top of the calorimeter, while the 90-degree location is pointed in the negative X-direction, toward the fire.

Temperatures were calculated for the center of each finite volume, but because of the choice in gridding for the model, the angular locations of the centers were not aligned with the locations of the thermocouples. Thus, the measured values at an angular location must be compared with the nearest calculated values. These angular groupings are listed in Table 3.

Figure 15 compares measured and calculated temperatures at the 90-degree location on the calorimeter (simulated cask). Both calculated transparent and absorbing gas results are shown with the measured values. The measured data have been shifted by 390 seconds in each plot to better synchronize the time for actual fire ignition with the calculated value. All of the surface temperatures shown were obtained by processing the measured and calculated temperature data through the SODDIT inverse heat transfer code. This produced the most accurate estimates of temperatures at the surface of the calorimeter.

TABLE 3. Angular positions of measured and calculated values.

Location of Measured Values	Nearest Locations for Calculated Values	
(degrees)	(degrees)	(degrees)
0	11.25	348.75
60	56.25	---
90	78.75	101.25
120	123.75	---
180	168.75	191.25
240	236.25	---
270	258.75	281.25

In Figure 16, the absorbing-gas calculations result in lower surface temperature predictions than do those for the transparent gas. This is true for all of the surface temperature comparisons. At the 90-degree location, the calculated temperature increases are greater than the measured increases. At the 60 and 270 degree angular positions, however, the calculated values nearly agree with the measured values.

The angular distributions of temperature and heat flux around the calorimeter were examined 9 and 18 minutes after fire ignition. These times were chosen so as to sample near the beginning and toward the end of the fire's duration. Figures 16 and 17 are plots of the surface temperature distribution around the calorimeter. At both times the measured temperatures are significantly less than the calculated temperatures, primarily in the region between 90 and 120 degrees from vertical.

Figure 18 compares air temperatures over time at a point about 6 m horizontally from the fire and 2.13 m vertically above the deck. In this case the absorbing-gas solution predicts air temperatures greater than the transparent-gas solution and is in better agreement with the measured values. With the hold vents open, the maximum calculated air temperatures 2.13 m above the deck were about 25°C lower than the closed-vent values shown in Figure 18.

Calorimeter Heat Fluxes. Figure 19 compares the heating rates at 90 degrees, derived from processing the calculated and measured temperature histories through the SODDIT code. On average, the calculated heat fluxes compare reasonably with the measured values for all locations.

Figures 20 and 21 show the distribution of heat flux around the calorimeter at 9 and 18 minutes. At 9 minutes, the modeled heat fluxes at 90 and 120 degrees are about 50% higher than the measured values, indicating that this simple crib fire model yields conservative results. However, at 18 minutes, they nearly agree with the measured values.

These comparisons of temperature and heat flux have shown that usable results can be obtained with rudimentary fire models. To achieve better agreement, more comprehensive fire models must be developed.

Flow Patterns. Figures 22 through 25 are streamline plots of the engine-room fire. Streamline plots are zero-mass particle tracks accumulated during the simulation. The streamline plots are based on seeding of the zero-mass particles. The seeding plane is parallel to the model plane-of-symmetry and passes through the midpoint of the calorimeter half.

Figures 22 and 23 show the flow patterns for the two-nozzle calculation. The figures show the development of fluid flow around the furnace and a plume above the calorimeter. A large convection cell is forming in the aft section of the hold. The convection cell is especially apparent in Figure 23.

Figures 24 and 25 show the flow patterns for the four-nozzle calculation. As in the two-nozzle calculation, fluid flow is developing around the furnace, and a plume above the calorimeter also formed, although the plume is not as obvious in the four-nozzle calculation. The lower ambient temperature of the four-nozzle calculation may contribute to the less prominent plume above the calorimeter. A large convection cell in the rear section of the hold also formed during the four-nozzle calculation.

The plots also show that the formation of the convection cell is a long-term event. The long formation time is an indicator of the relatively minor contribution of convection-heat transfer.

Surface Temperature Comparisons. The analytical and experimental data were compared at seven locations on the calorimeter (Figure 14). Three of the analytical temperature locations (60, 120 and 240 degrees from vertical) coincided with experimental thermocouple positions. The remaining four temperature comparisons (0, 90, 180 and 270 degrees from vertical) used the average analytical temperature from analytical temperature locations on either side of the experimental thermocouple location. The analytical temperature locations were 4.5 degrees on either side of the experimental thermocouple location.

Figure 26 is a time-temperature comparison, at 0, 60, and 90 degree locations on the calorimeter, for the two-nozzle model calculation and experimental data. The calculated temperatures are lower than the experimental temperatures, but are still a reasonable estimate. The distribution of temperatures between the experimental data and the calculated data shows similar trends. The 60- degree location has the highest temperature for both the experimental and calculated data, while the 0-degree location has the lowest temperature for both the experimental and analytical data. The plot also shows that the peak temperature occurs at the same time, 62 minutes, for both sets of data. The difference in temperature between the experimental data and analytical calculations could be caused by differences in hot-spot area, hot-spot position, flame temperature, or combinations of these three factors.

Figure 27 is a time-temperature plot at 120, 180, 240, and 270 degrees from vertical on the calorimeter for the two-nozzle model calculation. The peak temperature difference between the experimental and calculated temperatures is 2° C and occurs at 120 degrees from vertical on the calorimeter. The peak temperature occurs at the120 degree location for both the experimental data and the calculations. The peak temperature occurs at 65 minutes for both the experimental data and calculations.

Figure 28 is a time-temperature comparison, at 0, 60, and 90 degrees from vertical on the calorimeter, for the four-nozzle model calculation and experimental data. The peak temperature difference between the experimental and calculated temperatures is 1° C and occurs at the 60 degree location on the calorimeter. The calculation temperatures encompass the experimental temperatures with the calculated temperatures at the 90 degree location, which is lower than the experimental temperature data at that location. The temperature distribution indicates that either the hot-spot area or the hot-spot position or some combination of these differed from the experiment. The peak temperature occurs at the same 65-minute time for the calculated and experimental temperature data.

Figure 29 is a time-temperature plot at 120, 180, 240, and 270 degree locations on the calorimeter for the four-nozzle model calculation. The calculated temperatures are higher than the experimental data at the 120 degree calorimeter location. The remaining temperatures, at 180, 240, and 270 degree locations on the calorimeter, agree within 2° C of the experimental values.

Figures 30 and 31 are circumferential temperature plots at 30 minutes for the two- and four-nozzle cases. Because 30 minutes is half way through the burning time, this time was chosen to represent a typical circumferential temperature distribution. The peak calculated temperature for the two-nozzle case (Figure 30) is lower than the peak experimental temperature, but the temperature distribution is comparable. A shift in the maximum and minimum temperatures is probably caused by differences between actual and simulated hot spot areas and positions.

The peak calculated temperature for the four-nozzle case (Figure 31) is higher than the peak experimental temperature. The temperature distribution is similar for both calculated and experimental temperatures. Again, a shift in the location of the maximum and minimum temperature is observed between the two curves.

Heat Flux Comparisons. Figures 32 through 35 present calculated surface-heat-flux plots of the calorimeter. SODDIT was used to calculate the surface heat fluxes. The same code and procedure was used to calculate surface heat fluxes from the experimental data.

Figure 32 is the surface-heat-flux plot for the two-nozzle case. The calculated heat fluxes are of the same order of magnitude as the experimental data. Figure 33 is the surface-heat-flux plot of the four-nozzle case. Again, the heat fluxes are within the range of heat fluxes calculated from the experimental data.

Figures 34 and 35 are circumferential heat-flux plots. The heat fluxes are of the same order of magnitude as the experimental data. A shift in the maximum and minimum heat flux, similar to that observed in the circumferential temperature plots, is evident. The positional shift is probably a result of forward-bulkhead hot-spot area and position differences.

Radiation/Convection Heat Transfer Partitioning. The CFD model was used to estimate the partitioning of convection and conduction components of the overall heat-transfer mechanism and the importance of the radiative heat-transfer mechanism for heat transferred to the calorimeter. The partitioning was accomplished by removing buoyancy from the convection model and by the use of a small value of thermal conductivity for the air to minimize conduction. The calculations were made with the same Hold-5 computer model, boundary conditions, and other factors such as time step.

Figure 36 compares the calorimeter surface temperatures with and without convection of, and conduction through, the air. The plot indicates that convection is a minor contributor to the heat transfer that occurs in this problem because there is no appreciable difference between the two sets of temperature data. However, the plot also shows that convection occurs, and for other ship-fire problems or other locations in the hold, convection could be more significant. As seen in the streamline plots, a large convection cell formed in the aft part of the hold. If the calorimeter were located aft, convection could make a larger contribution to the overall heat transfer. Convection also contributes to the overall heat transfer mechanism just aft of the front bulkhead, where the hot spots are located. The convection driving potential is larger in this area due to the larger temperature difference between the air and heated surface.

Calculations show a recirculation cell occuring in front of the furnace near the overhead. The recirculation cell may cause some flow blockage over the top of the furnace, forcing the flow around the furnace. There is also a recirculation cell in front of the furnace near the deck. Part of the recirculation cell could cause the air flow observed beneath the calorimeter. A third recirculation cell occurs near the front bulkhead just above the midpoint between the deck and the overhead. Recirculation in this area would reduce convective heat transfer to the calorimeter. There is upward flow at the front bulkhead and above the calorimeter.

An upward flow of air above the calorimeter was observed in the experimental data by using flow visualization techniques. The temperature plots also reveal a plume formed above the calorimeter. The plume was caused by heating the calorimeter by the engine-room fire and in turn heating the local air, near the calorimeter, which caused convective flow to occur. Another feature of the flow is the recirculation occurring under the calorimeter.

The forward bulkhead hot spot is next to the king post. A second hot spot exists further away from the king post. Two of the recirculation cells that occurred in the two-nozzle case also occurred in the four-nozzle case. The recirculation cell, in the four-nozzle case, in front of the furnace near the overhead is larger than the corresponding recirculation cell in the two-nozzle case. The recirculation cell that was in front of the furnace and near the deck in the two-nozzle case moved forward and decreased in size. The recirculation cell that was near the front bulkhead in the two nozzle-case is not present, and another recirculation cell has formed directly

in front of the calorimeter. The latter is smaller than the recirculation cell near the front bulkhead in the two-nozzle case.

As in the two-nozzle case, upward flow occurs near the front bulkhead and above the calorimeter. Flow also occurs under the calorimeter. Upward flow was evident in the experimental data as well. A series of flow-visualization devices were constructed directly above the calorimeter. A review of the videotape of Hold 5 taken during the tests show the upward flow from the flow visualization devices.

CONCLUSIONS

Model simulations that accurately estimate a maritime fire environment for radioactive material packages can be developed from basic ship-hold geometry and a simplified fire-heating source. Overall, package-temperature estimates within 10 to 20°C are possible, and the locations and magnitudes of peak heat fluxes can also be successfully predicted. A package design based on such simulations would be expected to survive similar accidents at sea.

Radiative heat transfer dominates the hold-fire environment near the hot bulkhead. This was determined by effectively eliminating the convective heat transfer mechanism in the simulations, and then comparing the results to calculations that included convection. For the package locations studied, no significant difference in results was detected. This indicates that simpler models based only on radiative heat transfer and conduction could yield accurate predictions in the future. However, convection should not be ruled out entirely for every ship-hold thermal analysis. There could be localized regions, for example away from the fire location or hot bulkhead, where convection could contribute significantly to the heat-transfer process.

The simulations showed that the development of convection patterns in the hold was a relatively long-term process. Large convection cells did not develop in the aft end of Hold 5 until later in the one-hour fire simulation. Smaller convection cells formed near the forward bulkhead on a much shorter time scale. The long time scale for formation of convection cells at the aft end of the hold is another indicator that convective-heat transfer does not dominate during the initial part of the fire.

The analyses also showed that effective flame temperatures in the range of 800 to 1000°C, when coupled with estimates of fire heat release, can give heat fluxes and temperatures typical of the measured fire environment for the simulated radioactive material package. The agreement obtained with three different-sized fire sources shows that scaling to larger fires should be successful.

This analysis demonstrated that flow patterns can be estimated with reasonable accuracy using a course-mesh CFD ship-hold model. The simulation predicted the occurrence of flow patterns near the calorimeter similar to those observed during the experiment. In the simulation and experiment, there was an upward flow above the calorimeter. The simulation also predicted a heated fluid layer near the ceiling that increases in thickness as time passes. The increase in thickness of a heated fluid near the ceiling has been measured and observed during experiments.

Acknowledgements - Sandia National Laboratories is a multiprogram laboratory operated by Sandia Corporation, a Lockheed Martin Company, for the United States Department of Energy under Contract DE-ACO4-94AL85000. The authors wish to thank Caroline Souza, who assisted in preparing the manuscript.

REFERENCES

1. **"Study and Implementation Plan on Safety of Shipments of Plutonium by Sea."** *Section 2904 of the Energy Policy Act of 1991.* Washington, DC: U. S. Congress; 1992.

2. Koski, J. G. Bobbe, M. A. Arviso, S. D. Wix, D. E. Beene, Jr., R. Byrd, and J. Graupmann, *Experimental Determination of the Shipboard Fire Environment for Simulated Radioactive Material Packages* , SAND-0506. Albuquerque, NM: Sandia National Laboratories; March 1997.

3. Koski, S.D. Wix, and D.E. Beene, Jr. "Experimental Measurement of a Shipboard Fire Environment with Simulated Radioactive Materials Packages." *Very Large Scale Fires, ASTM STP 1336* , N.R. Keltner, N.J. Alvares, and S.J. Grayson, Eds. Philadelphia, PH: American Society for Testing Materials; 1998.

4. *CFX-F3D User Manual, Version 4.1* . Pittsburg, PA: AEA Technologies; October 1995.

5. Patankar, *Numerical Heat Transfer and Fluid Flow.* New York, NY: McGraw-Hill Book Company; 1980.

6. Jursa, A.S., ed. *Handbook of Geophysics and the Space Environment.* Springfield, VA: USAF Geophysics Laboratory, 1985.

7. Blackwell, R. W. Douglass, and H. Wolf, *A User's Manual for the Sandia One-Dimensional Direct and Inverse Thermal (SODDIT) Code* , SAND85-2478. Albuquerque, NM: Sandia National Laboratories; May 1987.

List of Captions

Figure 1. Schematic of the fire test arrangement

Figure 2. Hold arrangement of the Mayo Lykes.

Figure 3. Hold 4 plan.

Figure 4. Hold 5 plan.

Figure 5. Starboard half of Hold 4 in the *Mayo Lykes*.

Figure 6. Expanded view of wood crib and calorimeter.

Figure 7. Plan and elevation views of Hold 4 with dimension in meters.

Figure 8. Thermal model for wood crib fire, with dimensions in meters.

Figure 9. Heat flux temporal model for crib fire.

Figure 10. Function used to model absorbing gas.

Figure 11. Overall model and detail of Hold 5 model.

Figure 12. IR image of Hold 5 hot spot.

Figure 13. Comparison of air temperatures with two different time steps.

Figure 14. End view of calorimeter and positions of calculated and measured temperatures.

Figure 15. Cask surface temperatures for model and experiment near 90 degrees from top.

Figure 16. Model and experimental surface temperatures around cask at 9 minutes.

Figure 17. Model and experimental temperatures around cask at 18 minutes.

Figure 18. Model and experiment air temperatures at 2.13 m above deck of Hold 4.

Figure 19. Calorimeter heat flux for model and experiment near 90 degrees.

Figure 20. Model and experimental heat fluxes around calorimeter at 9 minutes.

Figure 21. Model and experimental heat fluxes around calorimeter at 18 minutes.

Figure 22. Two-nozzle flow pattern at 30 minutes.

Figure 23. Two-nozzle flow pattern at 60 minutes.

Figure 24. Four-nozzle flow pattern at 30 minutes.

Figure 25. Four-nozzle flow pattern at 60 minutes.

Figure 26. Two-nozzle temperature comparison at 0, 60, and 90 degrees.

Figure 27. Two-nozzle temperature comparison for 128, 180, 240, and 270 degrees.

Figure 28. Four-nozzle temperature comparison at 0, 60, and 90 degrees.

Figure 29. Four-nozzle temperature comparison for 120, 180, 240, and 270 degrees.

Figure 30. Two-nozzle circumferential temperature distribution at 30 minutes.

Figure 31. Four-nozzle circumferential temperature distribution at 30 minutes.

Figure 32. Two-nozzle heat flux comparison at 0, 60, and 90 degrees.

Figure 33. Four-nozzle heat flux comparison at 0, 60, and 90 degrees.

Figure 34. Two-nozzle circumferential heat flux distribution at 30 minutes.

Figure 35. Four-nozzle circumferential heat flux distribution at 30 minutes.

Figure 36.Comparison of the calorimeter surface temperature with and without convection of, and conduction through the fluid.

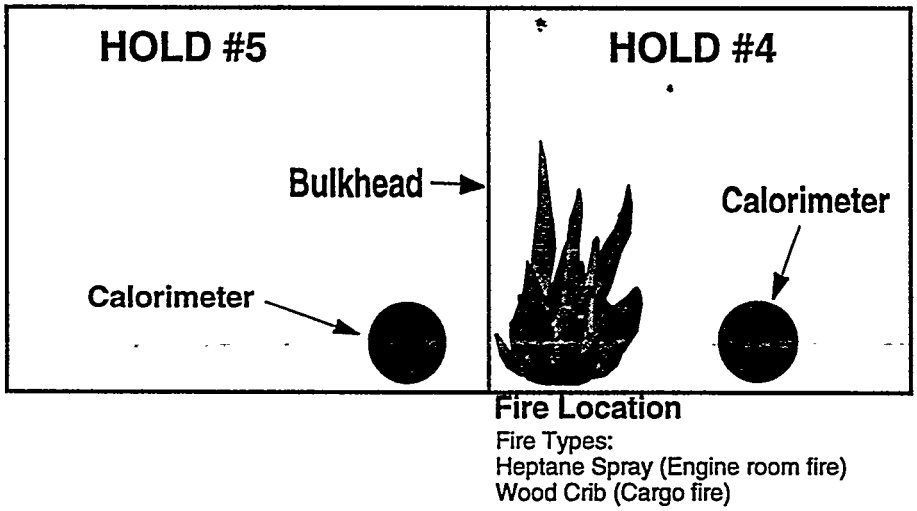

Figure 1. Schematic of the fire test arrangement.

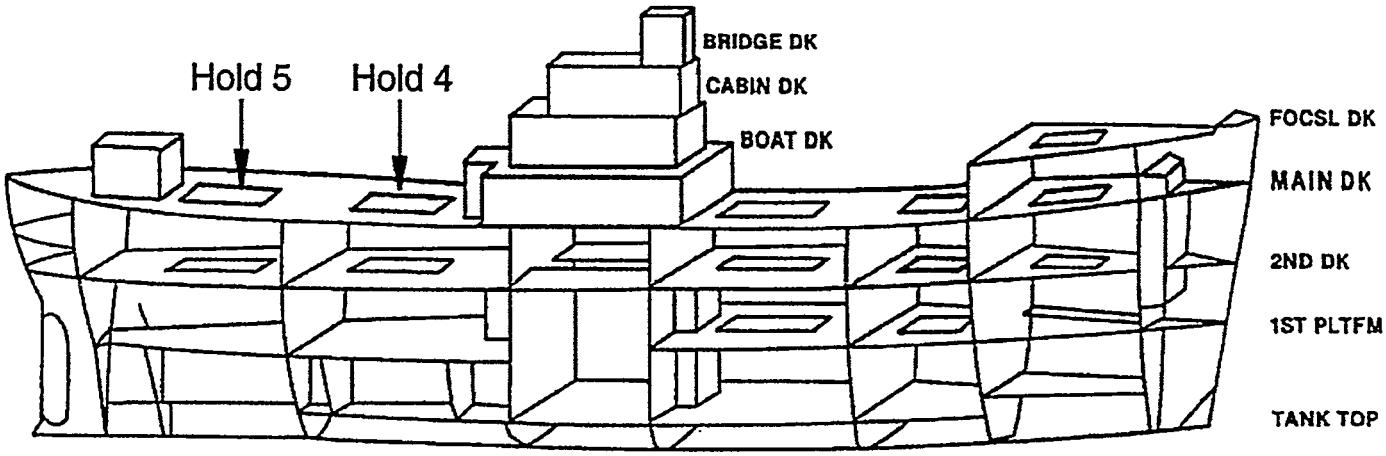

Figure 2. Hold arrangement of the Mayo Lykes.

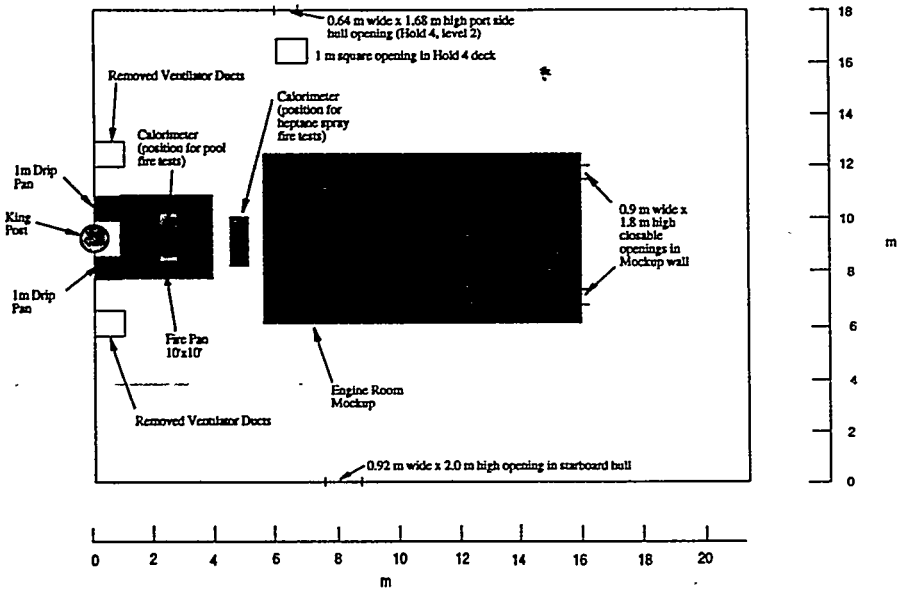

Figure 3. Hold 4 plan.

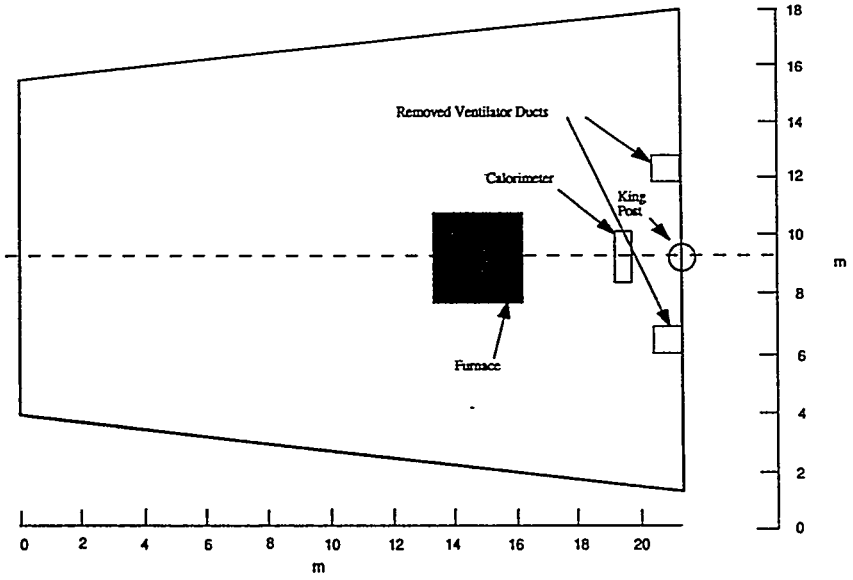

Figure 4. Hold 5 plan.

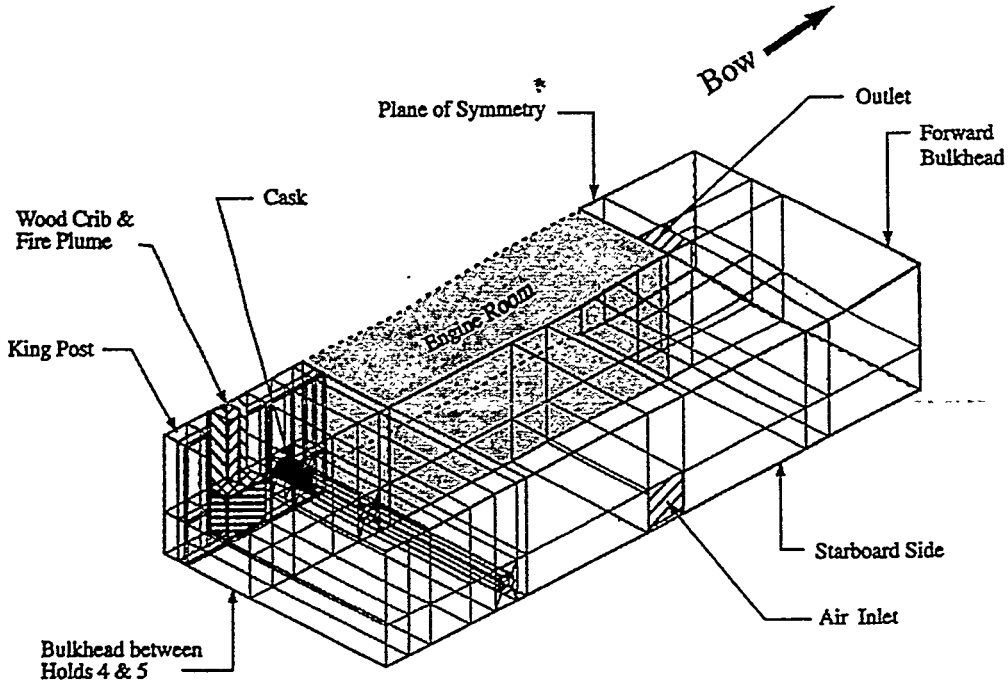

Figure 5. Starboard half of Hold 4 in the *Mayo Lykes*.

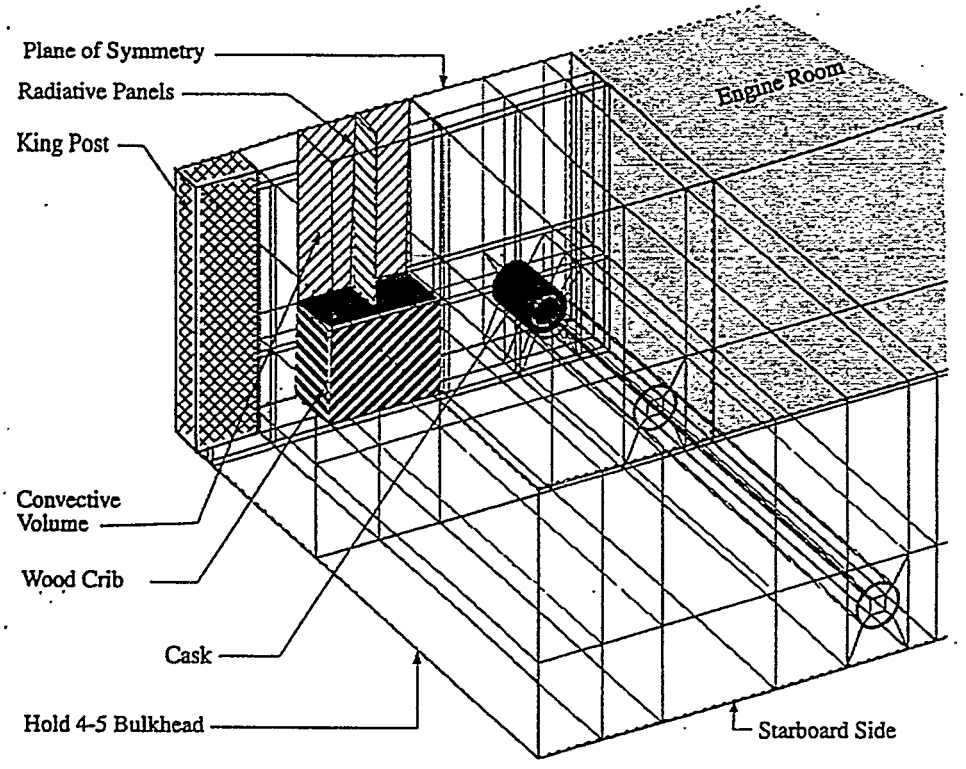

Figure 6. Expanded view of wood crib and calorimeter.

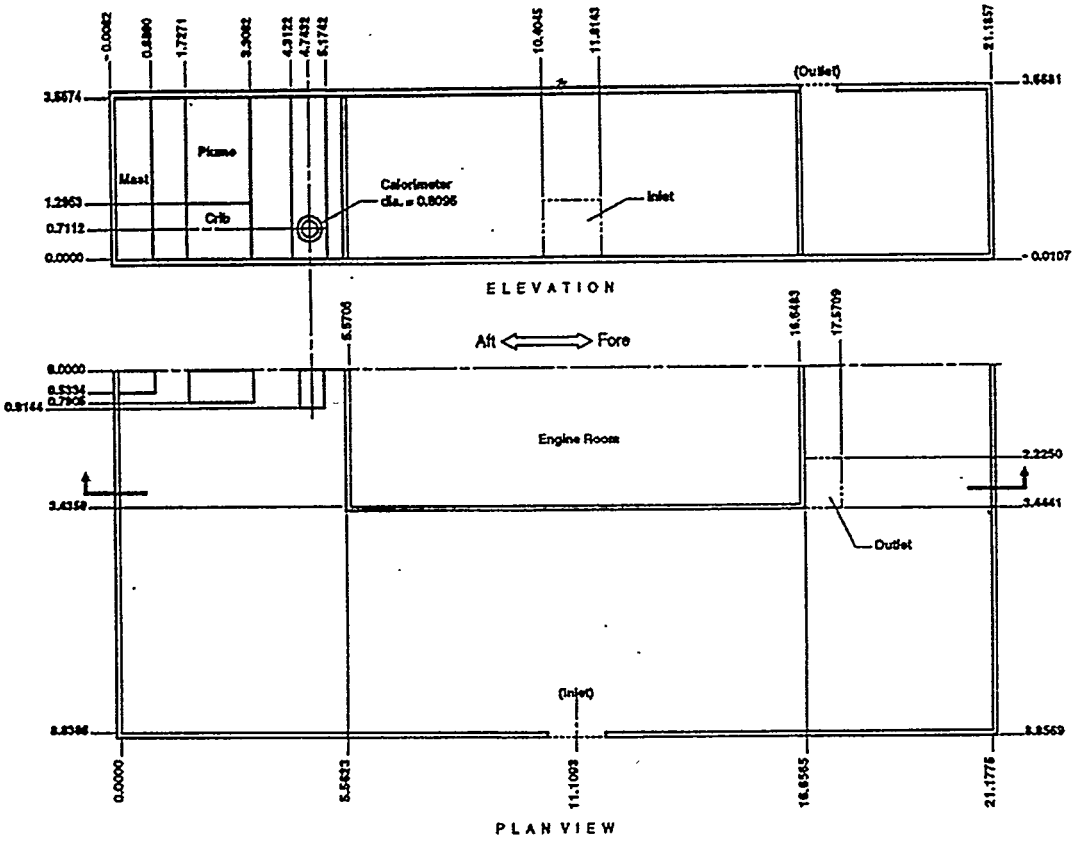

Figure 7. Plan and elevation views of Hold 4 with dimension in meters.

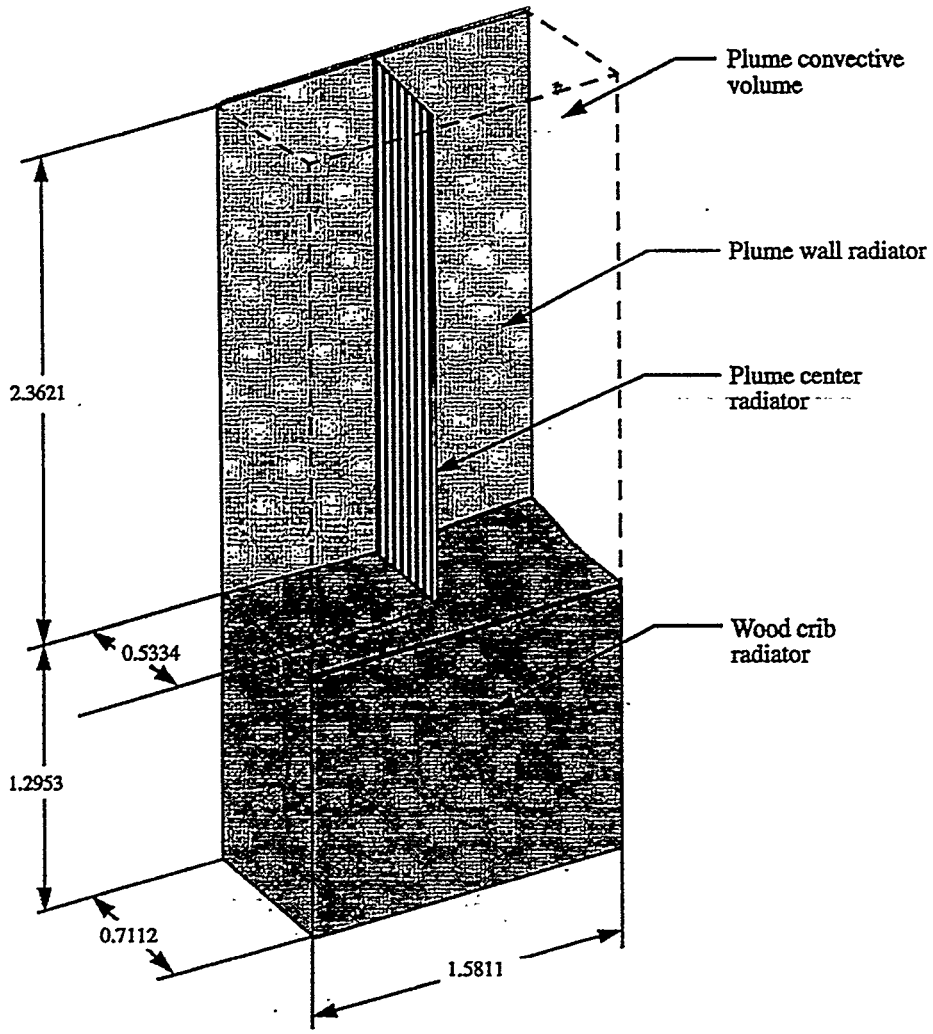

Figure 8. Thermal model for wood crib fire, with dimensions in meters.

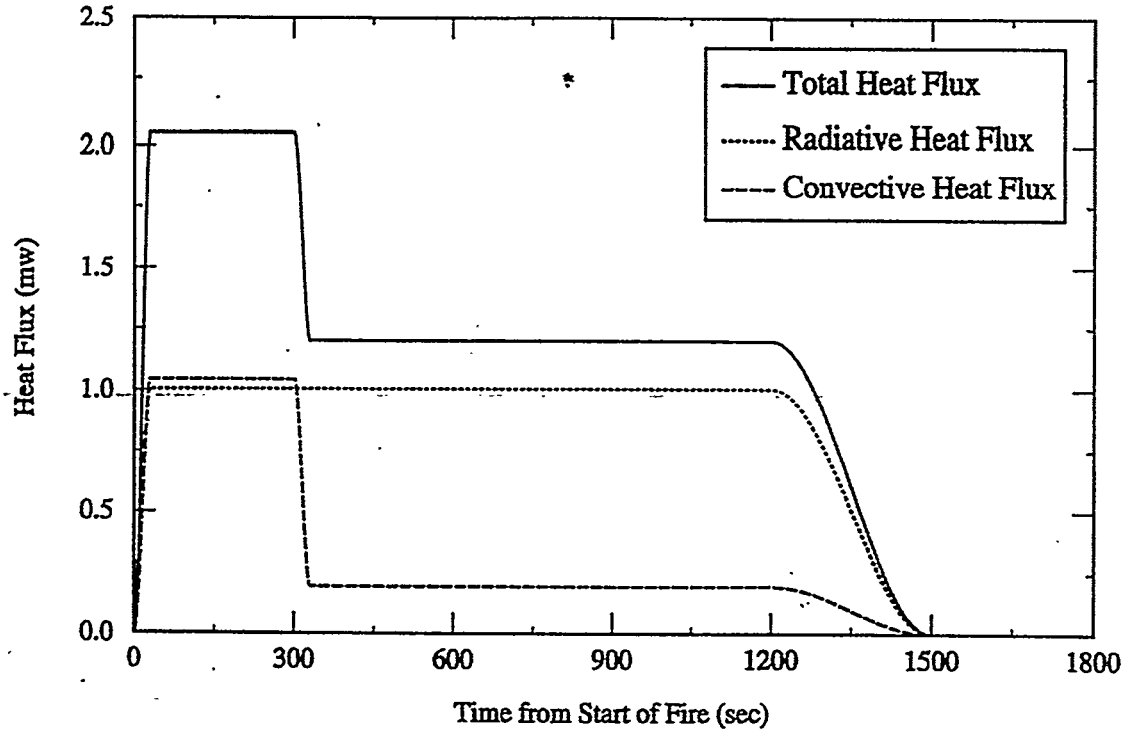

Figure 9. Heat flux temporal model for crib fire.

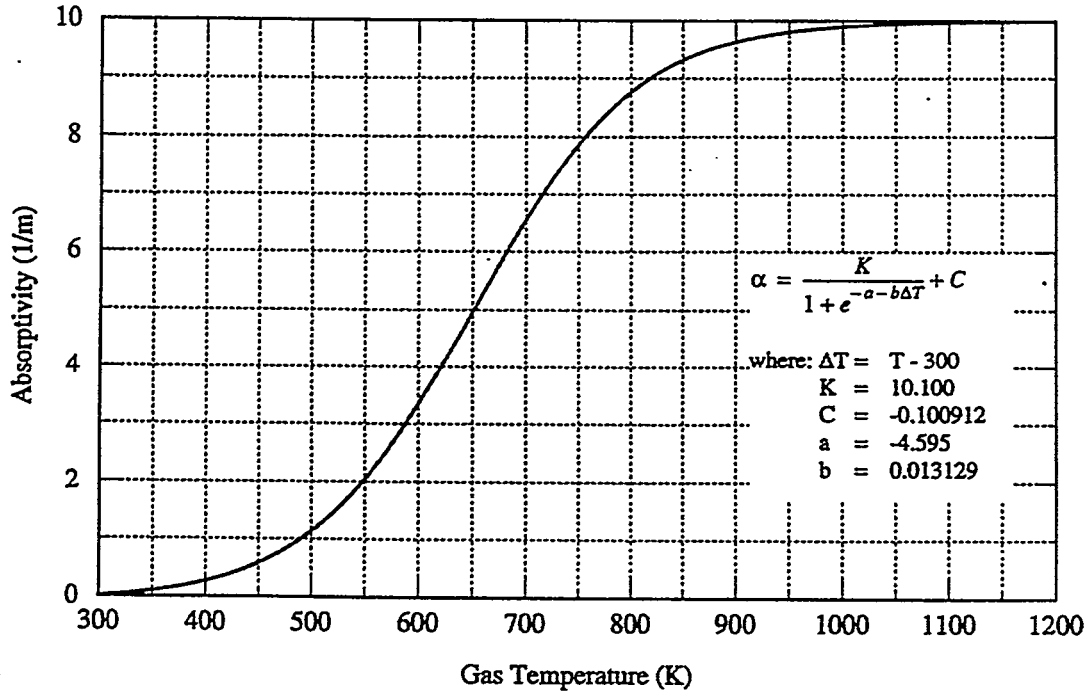

Figure 10. Function used to model absorbing gas.

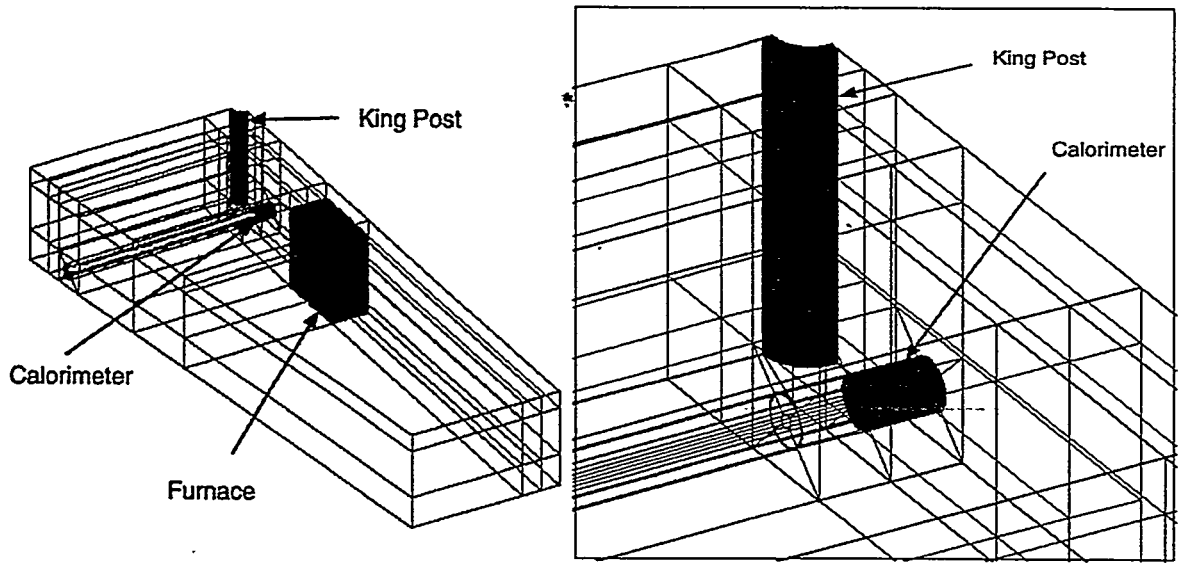

Figure 11. Overall model and detail of Hold 5 model.

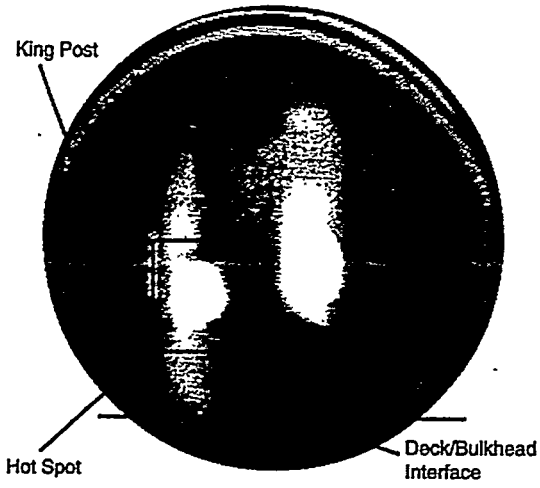

Figure 12. IR image of Hold 5 hot spot.

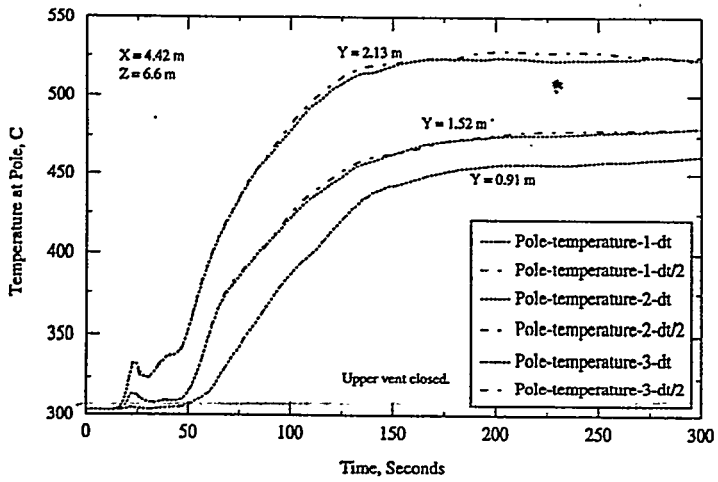

Figure 13. Comparison of air temperatures with two different time steps.

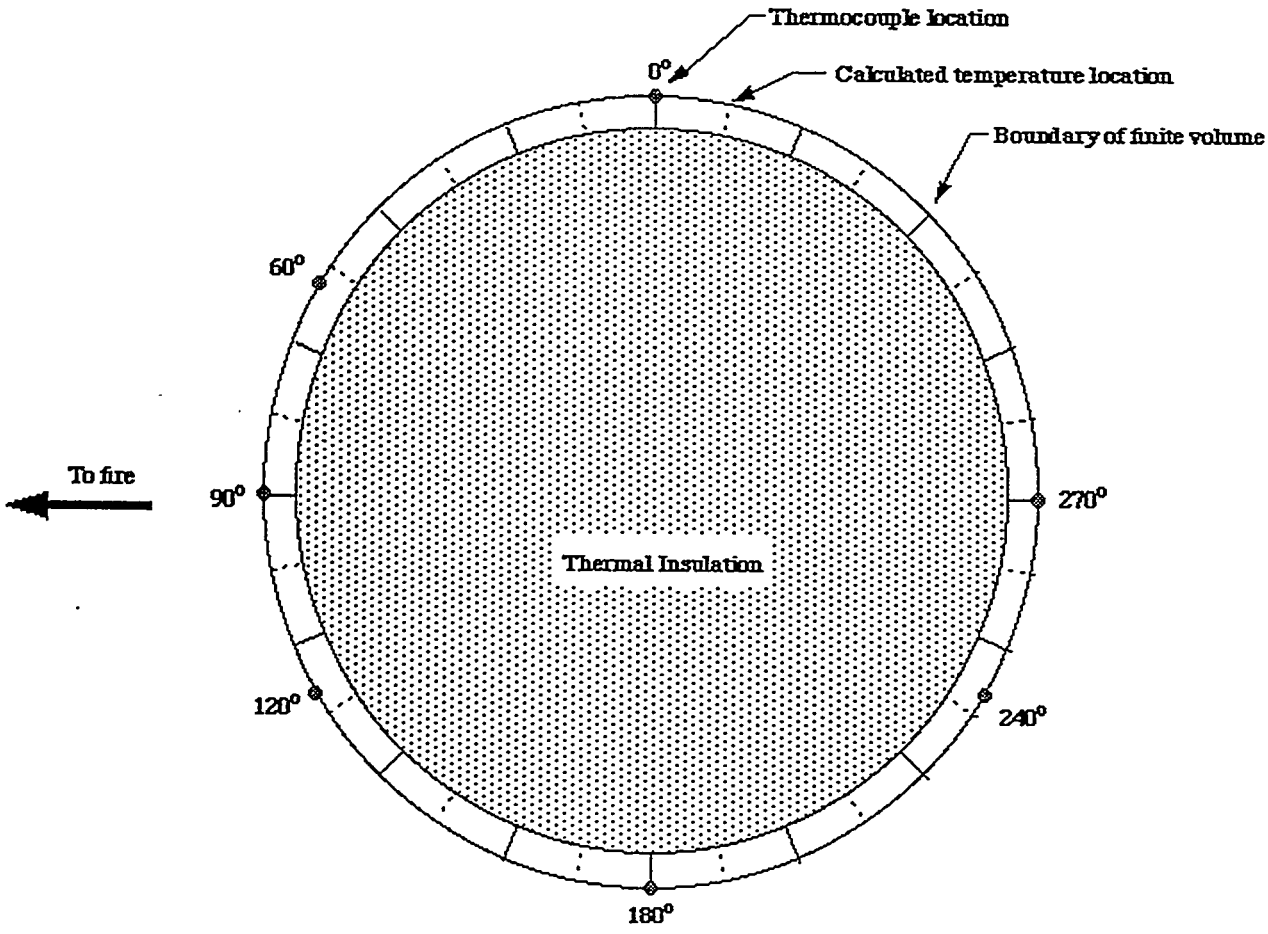

Figure 14. End view of calorimeter and positions of calculated and measured temperatures.

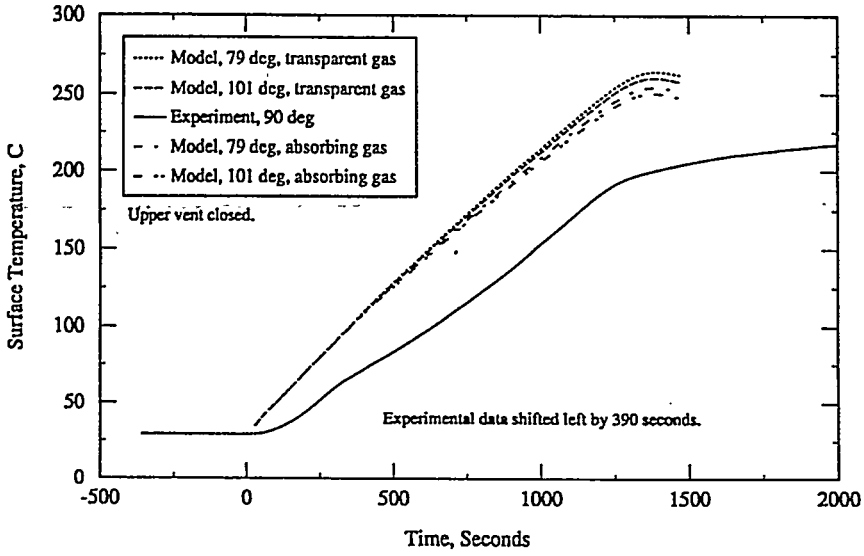

Figure 15. Cask surface temperatures for model and experiment near 90 degrees from top.

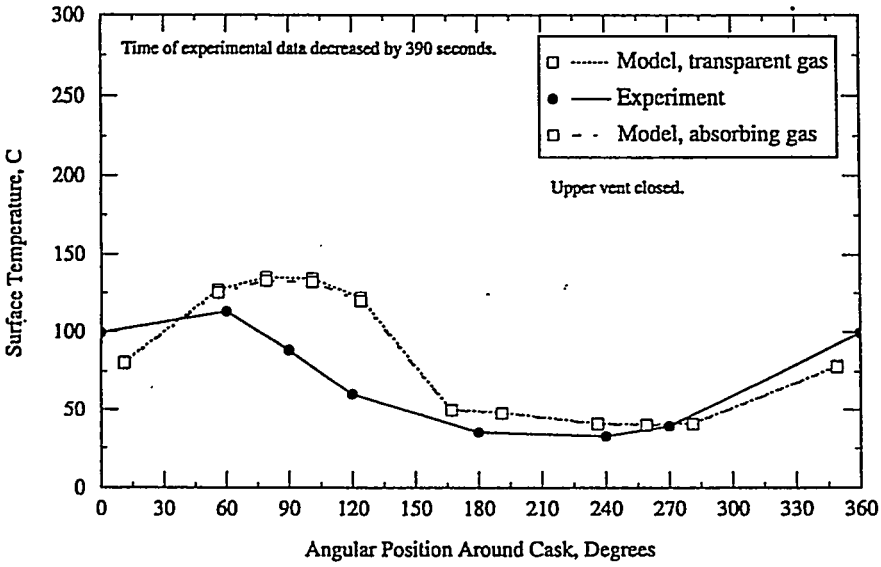

Figure 16. Model and experimental surface temperatures around cask at 9 minutes.

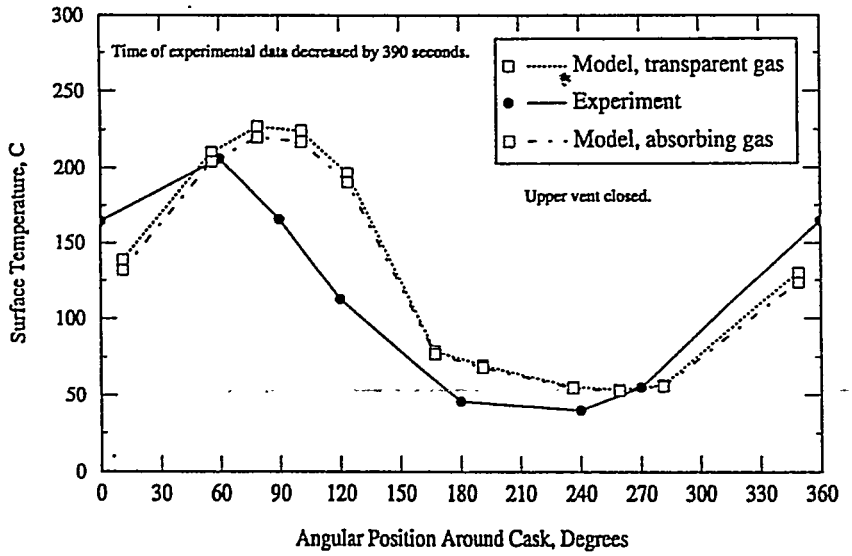

Figure 17. Model and experimental temperatures around cask at 18 minutes.

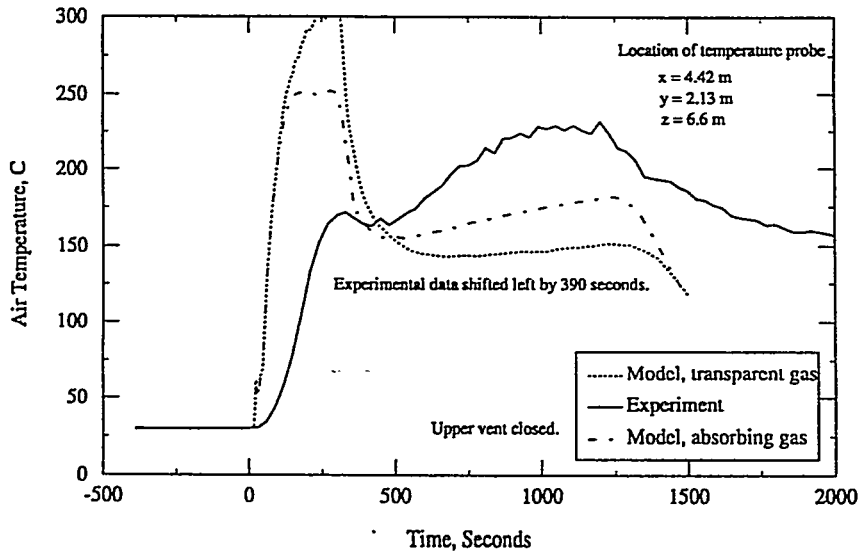

Figure 18. Model and experiment air temperatures at 2.13 m above deck of Hold 4.

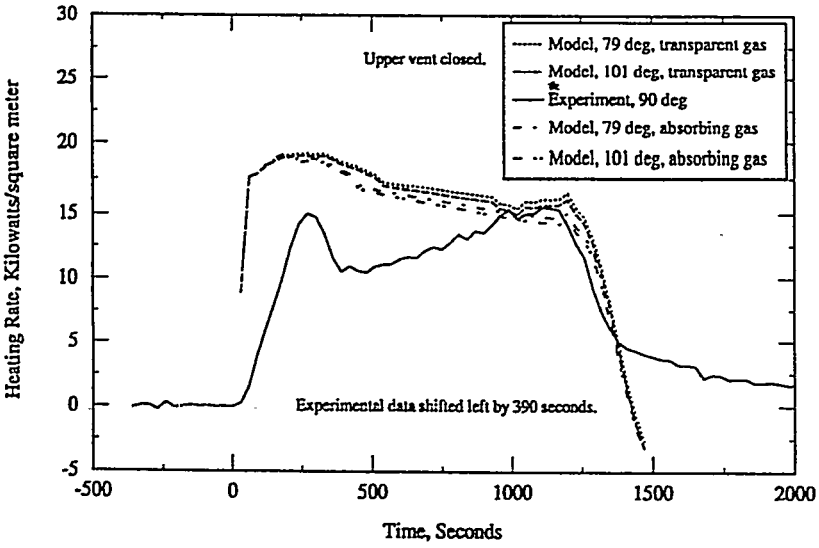

Figure 19. Calorimeter heat flux for model and experiment near 90 degrees.

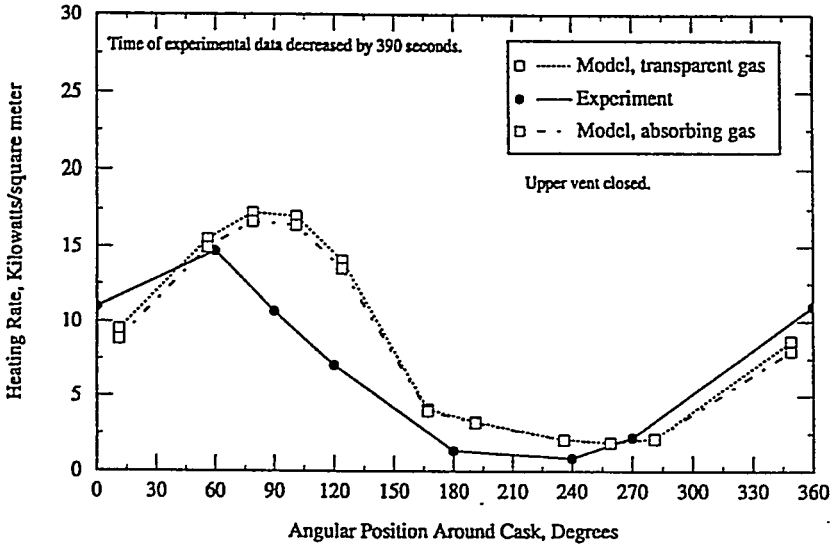

Figure 20. Model and experimental heat fluxes around calorimeter at 9 minutes.

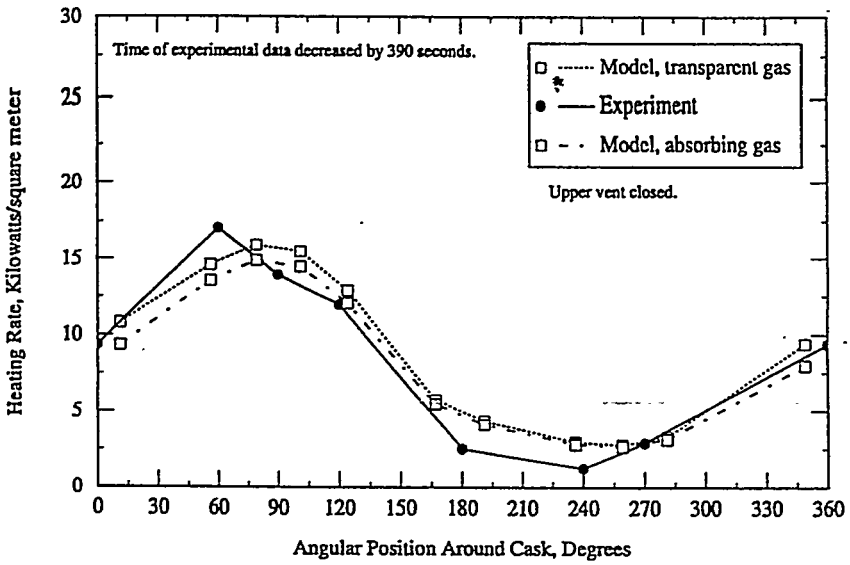

Figure 21. Model and experimental heat fluxes around calorimeter at 18 minutes.

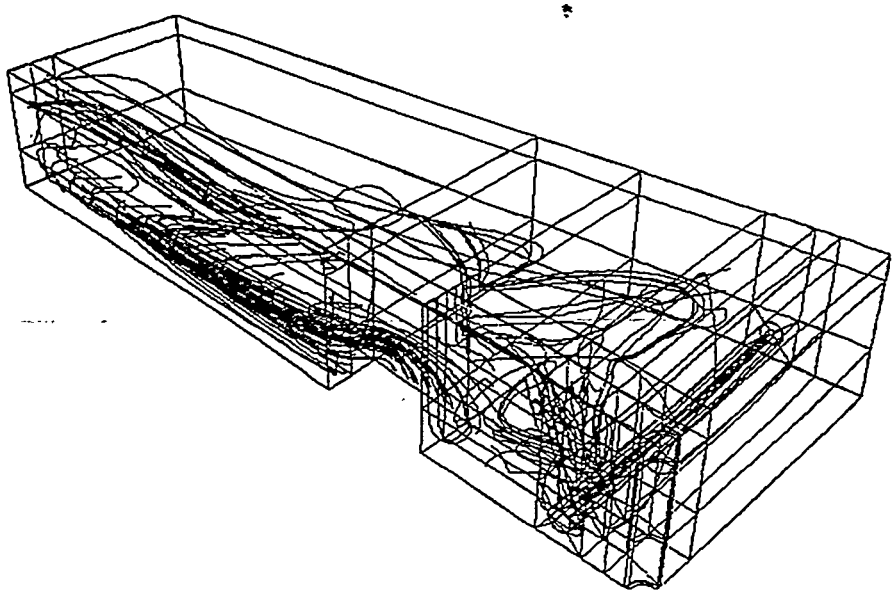

Figure 22. Two-nozzle flow pattern at 30 minutes.

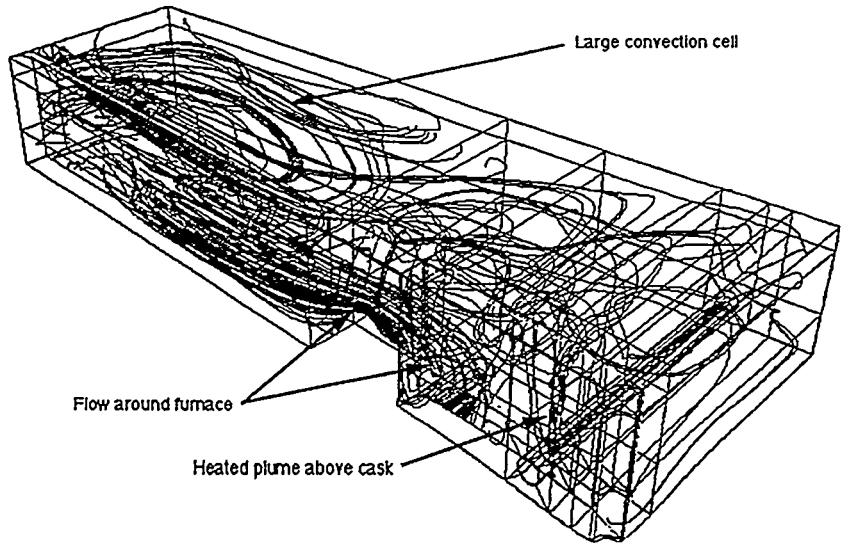

Figure 23. Two-nozzle flow pattern at 60 minutes.

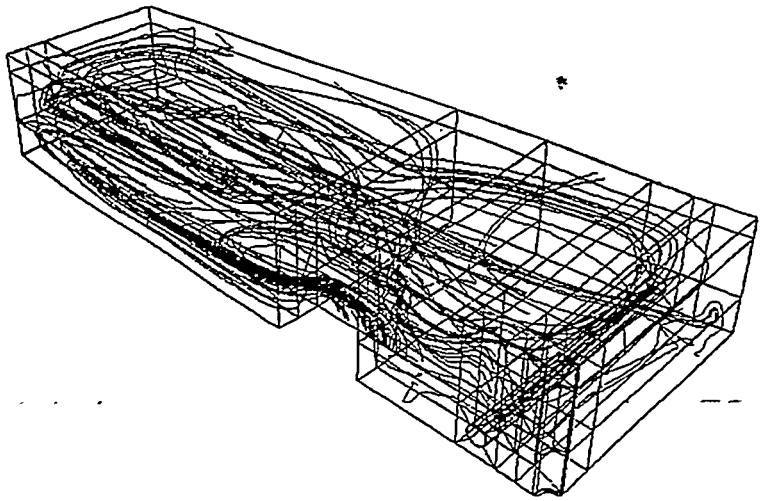

Figure 24. Four-nozzle flow pattern at 30 minutes.

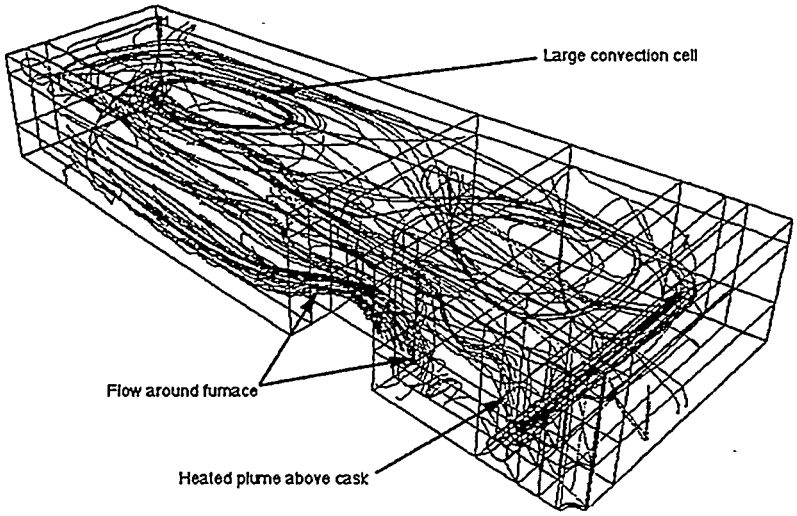

Figure 25. Four-nozzle flow pattern at 60 minutes.

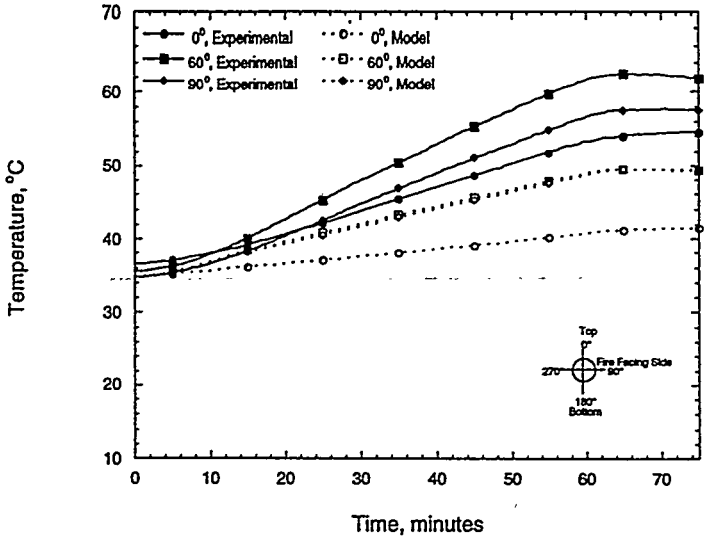

Figure 26. Two-nozzle temperature comparison at 0, 60, and 90 degrees.

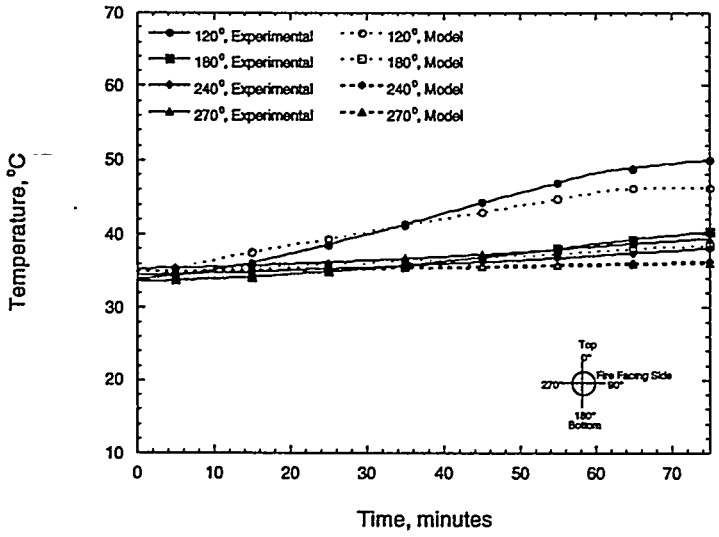

Figure 27. Two-nozzle temperature comparison for 128, 180, 240, and 270 degrees.

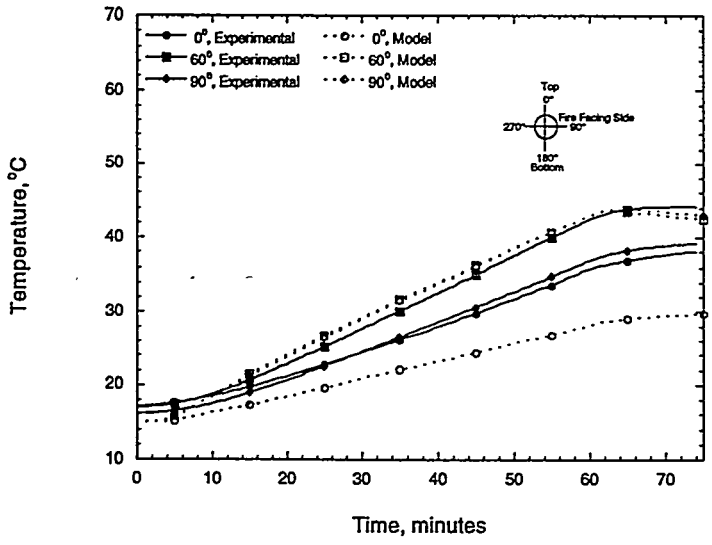

Figure 28. Four-nozzle temperature comparison at 0, 60, and 90 degrees.

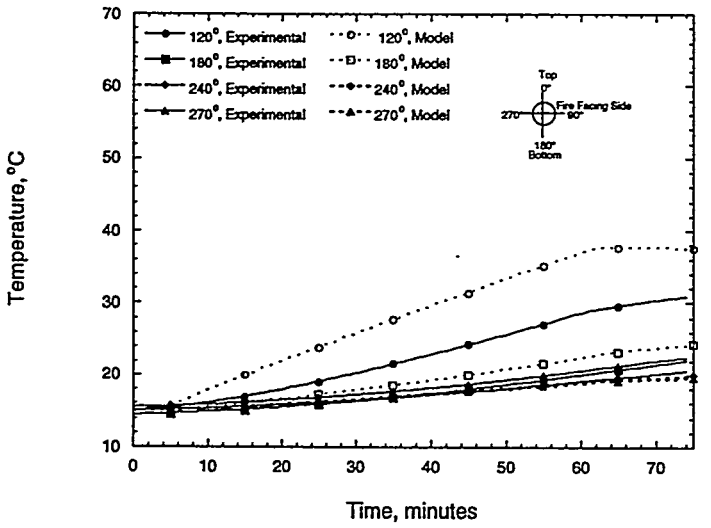

Figure 29. Four-nozzle temperature comparison for 120, 180, 240, and 270 degrees.

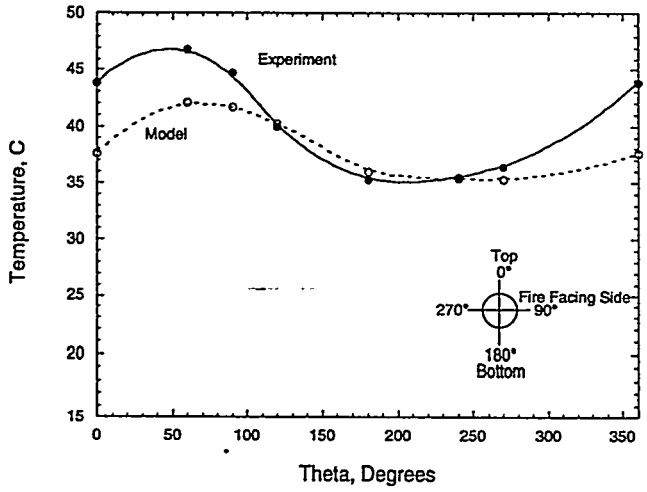

Figure 30. Two-nozzle circumferential temperature distribution at 30 minutes.

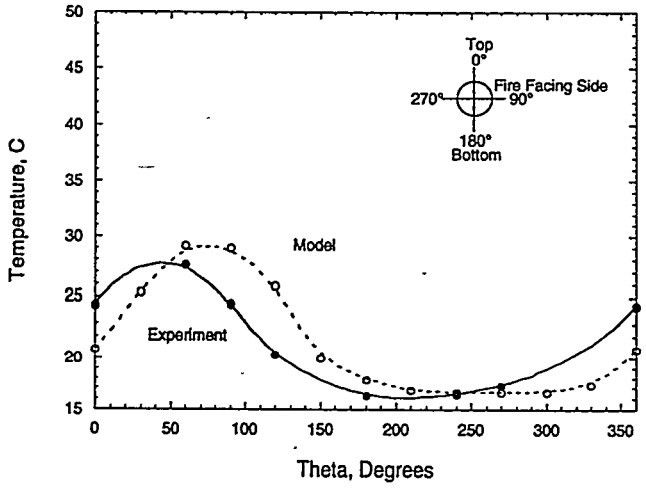

Figure 31. Four-nozzle circumferential temperature distribution at 30 minutes.

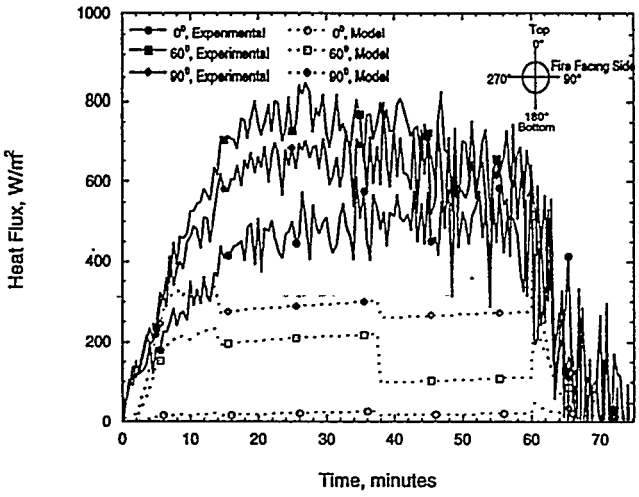

Figure 32. Two-nozzle heat flux comparison at 0, 60, and 90 degrees.

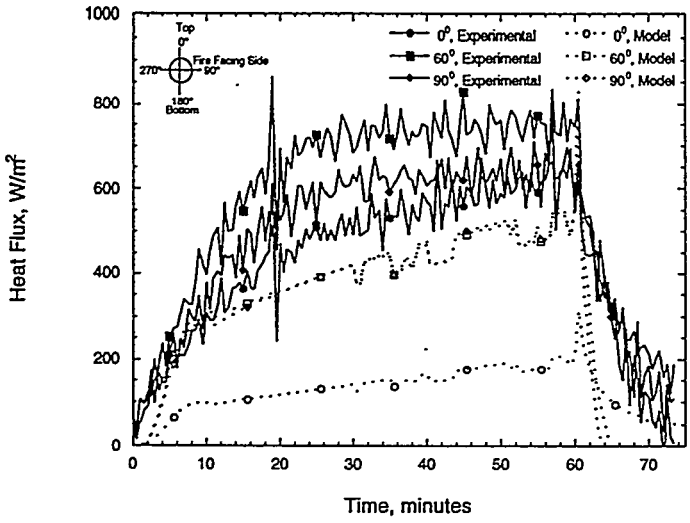

Figure 33. Four-nozzle heat flux comparison at 0, 60, and 90 degrees.

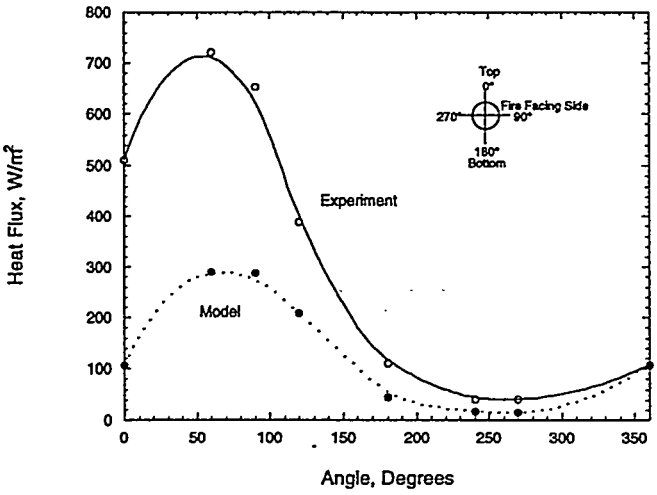

Figure 34. Two-nozzle circumferential heat flux distribution at 30 minutes.

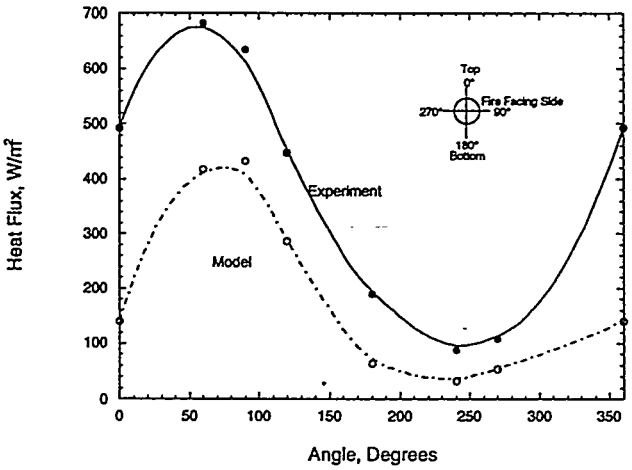

Figure 35. Four-nozzle circumferential heat flux distribution at 30 minutes.

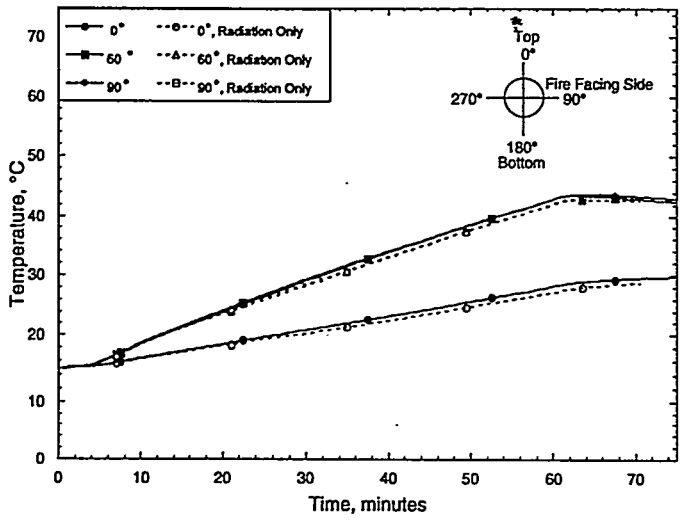

Figure 36.Comparison of the calorimeter surface temperature with and without convection of, and conduction through the fluid.